Lithium Insertion into Titanium Phosphates, Silicates, and Sulfates

Sébastien Patoux and Christian Masquelier*

Laboratoire de Réactivité et de Chimie des Solides, CNRS UMR 6007, Université de Picardie Jules Verne, 33 rue Saint-Leu, 80039 Amiens Cedex, France

Received May 29, 2002. Revised Manuscript Received September 10, 2002

Ti^{IV} phosphates, sulfates, and silicates were investigated as positive electrodes in lithium batteries. We present the lithium insertion into $TiSO_5$, $LiTiPO_5$, Li_2TiSiO_5, TiP_2O_7, and $ATi_2(PO_4)_3$ (A = Li, Na). The SO_4^{2-}, PO_4^{3-}, and SiO_4^{4-} groups alter significantly the operating voltage due to the inductive effect on the Ti^{4+}/Ti^{3+} redox couple lying around 2.5 V vs Li^+/Li, i.e., ∼1 V higher than for "simple" titanium oxides such as spinel $Li_4Ti_5O_{12}$ or $LiTiCrO_4$. Galvanostatic (GITT) and potentiostatic (PITT) intermittent titration techniques coupled with in situ X-ray diffraction were used to understand the lithium insertion mechanisms into these materials. Chemical lithiation was also performed on TiP_2O_7 and $ATi_2(PO_4)_3$ (A = Li, Na) to isolate new Ti^{III}-based compositions.

1. Introduction

Research for materials that would provide lighter batteries with higher energy density is the consequence of increasing consumer demands on numerous portable technologies (computers, cell phones, etc.). For the last five years, a new generation of positive electrode materials based on 3-D phosphate opened-frameworks that reversibly insert lithium was proposed, following the pioneering works of Padhi et al.[1,2] These materials take advantage of a relatively high lithium ion mobility and benefit from the inductive effect generated by the polyanionic groups, which increase the operating voltage in comparison with simple oxides.[3−5] In this context, much attention was given to phosphates[6,7] and sulfates[8,9] of iron or vanadium. Good reversibility was demonstrated for the Fe^{3+}/Fe^{2+} couple in cheap and nontoxic iron-containing materials such as $Fe_2(SO_4)_3$ (3.6 V), $LiFePO_4$ (3.45 V), and $Li_3Fe_2(PO_4)_3$ (2.8 V).

Only very little is known so far of the behavior of Ti^{4+}-containing polyanionic materials toward lithium insertion, besides the early works of Delmas in the late 1980s[10,11] on NASICON $A_{1+x}Ti_2(PO_4)_3$ (A = Li, Na) and recent contributions from the same group.[12] Despite the low intrinsic electronic conductivity of these 3-D phosphates, which was pointed out by Delmas[10,11] as a major drawback for possible applications, they still deserve attention in light of progress that has been communicated recently on how to make them work efficiently at high current densities through "smart" conductive carbon coating.[13−15] The slightly lighter molecular weight of titanium as compared to that of iron induces a higher theoretical specific capacity than for iron isostructural materials: 138 mAh/g for $Li_{1+x}Ti_2(PO_4)_3$, and 128 mAh/g for $Li_3Fe_2(PO_4)_3$. Additionally, titanium is also environmentally benign, as its derivative compounds are usually easy to prepare.

Many authors reported the excellent reversibility of the $Ti^{4+/3+}$ redox couple in simple oxides, such as the spinel $Li[Li_{1/3}Ti_{5/3}]O_4$, for instance. Below is the summary of the redox behavior of simple Ti^{IV} oxides already reported in the literature.

As shown in Figure 1a, only 0.5 lithium, instead of one in theory (Ti^{4+} to Ti^{3+}) can be reversibly inserted into the cubic close-packed arrangement of anatase TiO_2 (in agreement with the literature[16,17]) with significant polarization. GITT shows that the position of the $Ti^{4+/3+}$

* To whom correspondence should be addressed: christian.masquelier@sc.u-picardie.fr.

(1) Padhi, A. K.; Nanjundaswamy, K. S.; Goodenough, J. B. *J. Electrochem. Soc.* **1997**, *144*, 1188−1194.
(2) Padhi, A. K.; Ph.D. Thesis, The University of Texas at Austin, 1997.
(3) Padhi, A. K.; Nanjundaswamy, K. S.; Masquelier, C.; Goodenough, J. B. *J. Electrochem. Soc.* **1997**, *144*, 2581−2586.
(4) Goodenough, J. B.; Manivannan, V. *Denki Kagaku*, **1998**, *66*, 1173−1181.
(5) Nanjundaswamy, K. S.; Padhi, A. K.; Goodenough, J. B.; Okada, S.; Ohtsuka, H.; Arai, H.; Yamaki, J. *Solid State Ionics* **1996**, *92*, 1−10.
(6) Padhi, A. K.; Nanjundaswamy, K. S.; Masquelier, C.; Okada, S.; Goodenough, J. B. *J. Electrochem. Soc.*, **1997**, *144*, 1609−1613.
(7) Andersson, A. S.; Thomas, J. O.; Kalska, B.; Häggström, L. *Electrochem. Solid-State Lett.* **2000**, *3*, 66−68.
(8) Padhi, A. K.; Manivannan, V.; Goodenough, J. B. *J. Electrochem. Soc.* **1998**, *145*, 1518−1520.
(9) Okada, S.; Nanjundaswamy, K. S.; Manthiram, A.; Goodenough, J. B.; Ohtsuka, H.; Arai, H.; Yamaki, J. *Presented at the 36th Power Sources Conference*, June 6−9, 1994; PSC Publication Commitee: Red Bank, NJ, 1994.
(10) Delmas, C.; Nadiri, A.; Soubeyroux, J. L. *Solid State Ionics* **1988**, *28−30*, 419−423.
(11) Delmas, C.; Nadiri, A. *Mater. Res. Bull.* **1988**, *23*, 65−72.
(12) Ménétrier, M. Personal communication, GFECI, March 2002, Orléans, France; Aatiq, A.; Ménétrier, M.; Croguennec, L.; Suard, E.; Delmas, C. *J. Mater. Chem.* **2002**; submitted for publication.
(13) Ravet, N.; Chouinard, Y.; Magnan, J. F.; Besner, S.; Gaulthier, M.; Armand, M. *J. Power Sources* **2001**, *97−98*, 503−507.
(14) Huang, H.; Yin, S.-C.; Nazar, L. F. *Electrochem. Solid State Lett.* **2001**, *4*, 170−172.
(15) Morcrette, M.; Wurm, C.; Masquelier, C. *Solid State Sci.* **2002**, *4*, 239−246.
(16) Zachau-Christiansen; West, K.; Jacobsen, T.; Atlung, S. *Solid State Ionics* **1988**, *28−30*, 1176.
(17) Zachau-Christiansen; West, K.; Jacobsen, T.; Skaarup, S. *Solid State Ionics* **1992**, *53−56*, 364−389.

10.1021/cm0201798 CCC: $22.00
Published on Web 11/19/2002

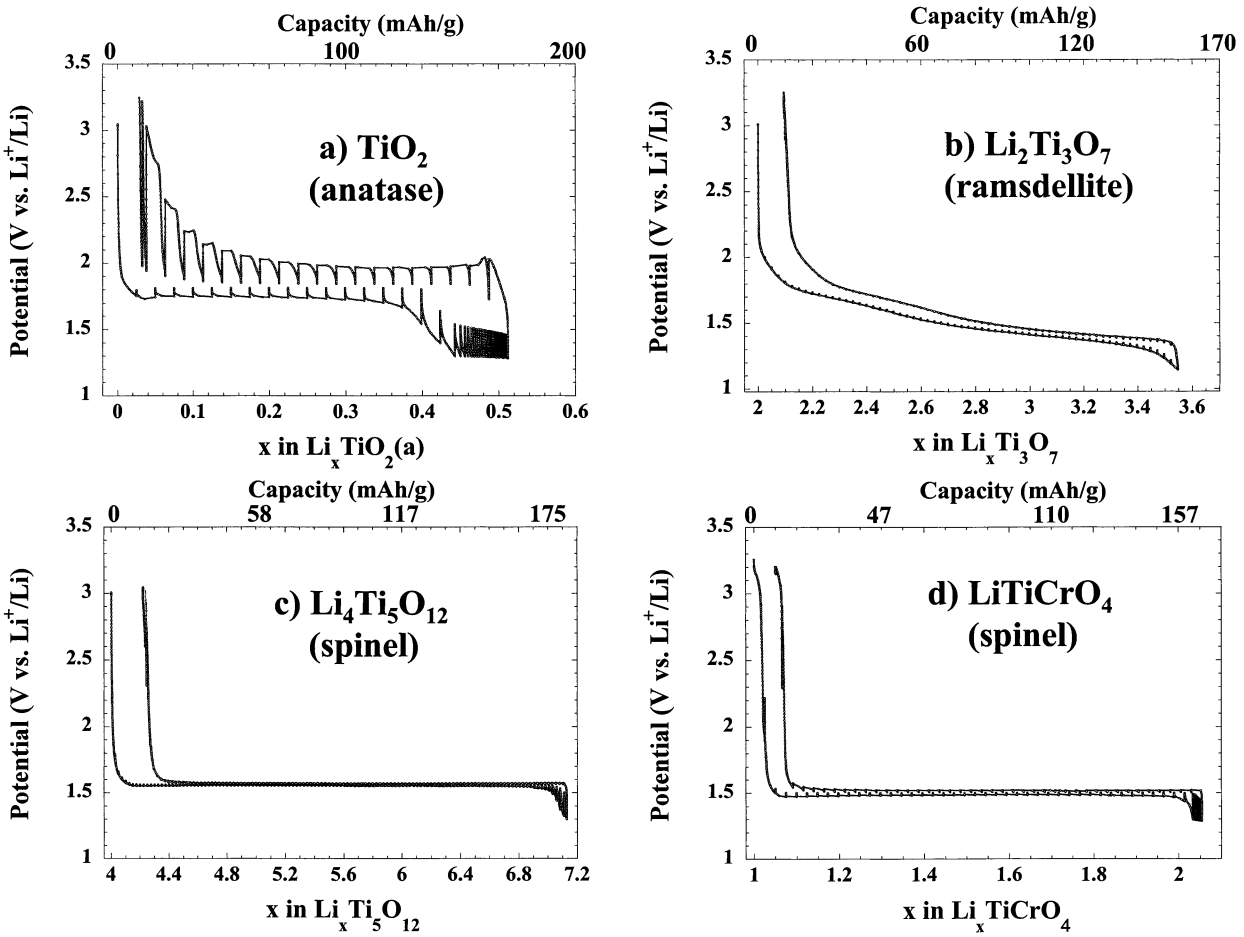

Figure 1. Potential−composition curves of (a) TiO_2 (anatase), (b) $Li_2Ti_3O_7$, (c) $Li_4Ti_5O_{12}$, and (d) $LiTiCrO_4$ obtained in galvanostatic intermittent mode: regime of C/20 for 30 min and relax periods of 30 min.

redox couple in TiO_2 anatase is 1.83 V vs Li^+/Li,[18] among the highest observed for titanium oxides.

The situation is much different for the ramsdellite $Li_2Ti_3O_7$ (Figure 1b) that can insert ~1.5 lithium ions per formula unit (0.5 Li per Ti) down to 1.2 V vs Li^+/Li.[19] The potential−composition profile is similar to that of ramsdellite TiO_2 (not presented here). The ramsdellite form of $Li_2Ti_3O_7$ may be alternatively described as $Li_{0.43}[Li_{0.14}Ti_{0.86}]O_2$ where 0.14 lithium is randomly distributed within the TiO_6 octahedra network, and 0.43 lithium already occupies the tetrahedral interstitial space. The remaining "empty space" for lithium insertion (equivalent to 0.57) leads to the theoretical reduction of $^2/_3$ of Ti^{IV} to Ti^{III} ((1 − 0.43)/0.86).

For the layered material Li_2TiO_3 ,[20] we observed no possible lithium insertion. This may be easily understood as all the octahedral interstices of the oxygen close-packed arrangement are already filled with lithium and titanium.

The exceptional stability of the spinel $Li_4Ti_5O_{12}$ ($Li^{(8a)}[Li_{1/3}Ti_{5/3}]^{(16d)}O_4$) toward lithium insertion/extraction is well documented in the literature.[21−24] Three electrons are exchanged in a two-phase reaction, with absolutely no polarization, between $Li_4Ti_5O_{12}$ and $Li_7Ti_5O_{12}$ at 1.52V vs Li^+/Li (Figure 1c). Migration of lithium ions occurs from the tetrahedral (8a) sites to the octahedral (16c) sites and the composition at the end of discharge was expressed by Ohzuku as $Li_2^{(16c)}[Li_{1/3}Ti_{5/3}]^{(16d)}O_4^{(32e)}$.[22] In terms of capacity, this reaction corresponds to 0.6 lithium inserted per transition metal element in the spinel structure. Remarkably, the excellent retention capacity of this material is correlated with an extremely small unit-cell volume variation between the two end-members of the two-phase domain.[21]

At the same voltage vs Li^+/Li, and following an insertion mechanism similar to that for $Li_{4+x}Ti_5O_{12}$, the normal spinel $Li[CrTi]O_4$[25] can insert one lithium ion per titanium element (0.5 lithium inserted per transition metal) (Figure 1d). The complete reduction of the Ti^{IV} to Ti^{III} is achieved without contribution of Cr^{III} to the redox process. Note that the isotypic $Li[FeTi]O_4$[26] only inserts 0.5 lithium per two transition elements and that only iron is reduced.

It appears then, as already documented in the literature, that a few Ti^{IV} oxides show excellent reversibility

(18) Kuhn, A.; Amandi, R.; Garcia-Alvarado, F. *J. Power Sources* **2001**, *92*, 221−227.
(19) Gover, R. K. B.; Tolchard, J. R.; Tukamoto, H.; Murai, T.; Irvine, J. T. S. *J. Electrochem. Soc.* **1999**, *146*, 4348−4353.
(20) ICSD Collection Code 15150: Li_2TiO_3.
(21) Scharner, S.; Weppner, W.; Schmid-Beurmann, P. *J. Electrochem. Soc.* **1999**, *146*, 857−861.
(22) Ohzuku, T.; Ueda, A.; Yamamoto, N. *J. Electrochem. Soc.* **1995**, *142*, 1431−1435.
(23) Wang, G. X.; Bradhurst, D. H.; Dou, S. X.; Liu, H. K. *J. Power Sources*, **1999**, *83*, 156−161.
(24) Zaghib, K.; Simoneau, M.; Armand, M.; Gaulthier, M. *J. Power Sources*, **1999**, *81−82*, 300−305.
(25) Ohzuku, T.; Tatsumi, K.; Matoba, N.; Sawai, K. *J. Electrochem. Soc.* **2000**, *147*, 3592−3597.
(26) Robertson, A. D.; Tukamoto, H.; Irvine, J. T. S. *J. Electrochem. Soc.* **1999**, *146*, 3958−3962.

Table 1. Structural Parameters and Redox Potentials vs Li^+/Li of the Titanium-Containing Compositions Investigated

formula	structure	space group	Z	a (Å)	b (Å)	c (Å)	V (Å^3)	E (V vs Li^+/Li)	ref.
TiO_2	anatase	I_{41}/amd	4	3.785	3.785	9.514	136	1.83	16, 17
$Li_2Ti_3O_7$	ramsdellite	$Pbnm$	1	5.017(1)	9.550(2)	2.945(1)	141(1)	2.3−1.2	19
Li_2TiO_3	layered	$C2/c$	8	5.070(1)	8.771(2)	9.749(3)	427(1)	no	no
$Li_4Ti_5O_{12}$	spinel	$Fd\bar{3}m$	8	8.364(1)	8.364(1)	8.364(1)	585(1)	1.56	22
$LiCrTiO_4$	spinel	$Fd\bar{3}m$	8	8.313(1)	8.313(1)	8.313(1)	574(1)	1.50	25
$LiFeTiO_4$	spinel	$Fd\bar{3}m$	8	8.362(1)	8.362(1)	8.362(1)	585(1)	2.25 (Fe)	26
Li_2TiSiO_5	oxotitanate	$P4/nmm$	2	6.437(1)	6.437(1)	4.400(1)	182(1)	No	this work
$LiTiPO_5$	oxotitanate	$Pnma$	4	7.406(1)	6.379(1)	7.238(1)	342(1)	1.51	this work
$TiSO_5$	ReO_3-type	$Pnma$	4	10.948(5)	5.144(2)	6.427(3)	362(1)	3.2−1.5	this work
TiP_2O_7	diphosphate	$Pa\bar{3}$	108	23.632(1)	23.632(1)	23.632(1)	13198(1)	2.62 and 2.55	this work
$LiTi_2(PO_4)_3$	NASICON	$R\bar{3}c$	6	8.508(1)	8.508(1)	20.833(6)	1306(1)	2.48	11
$NaTi_2(PO_4)_3$	NASICON	$R\bar{3}c$	6	8.478(1)	8.478(1)	21.786(3)	1356(1)	2.4	this work

toward lithium insertion/extraction on the Ti^{4+}/Ti^{3+} couple, located between 2.00 and 1.5 V vs Li^+/Li. Interestingly, the spinels $Li_4Ti_5O_{12}$ and $LiTiCrO_4$ show basically no polarization with attractive practical capacities of ∼160−170 mAh/g and redox potentials that make them interesting as negative electrodes in Li-ion cells.

We decided to embark on the preparation and electrochemical study of many titanium phosphates, sulfates, and silicates with the objectives of (1) identifying new alternative materials with attractive properties, (2) studying how the crystal structure and the nature of the $(XO_4)^{n-}$ groups would affect the Ti^{4+}/Ti^{3+} redox potential, and (3) relating their electrochemical behavior to structural changes that occur on cycling. We present an investigation of electrochemical lithium or sodium insertion in $TiSO_5$, $LiTiPO_5$, Li_2TiSiO_5, TiP_2O_7, $LiTi_2(PO_4)_3$, and $NaTi_2(PO_4)_3$, compared with titanium oxides such as TiO_2 (anatase), $LiTiCrO_4$ (spinel), $Li_4Ti_5O_{12}$ (spinel), and $Li_2Ti_3O_7$ (ramsdellite). Particular attention will be given to $A_xTi_2(PO_4)_3$ (A = Li, Na) and $Li_xTiP_2O_7$ compositions that were investigated by various electrochemical cycling modes (galvanostatic or potentiostatic), in situ X-ray diffraction, and chemical lithiation.

2. Experimental Section

Most of the polycrystalline materials were synthesized by solid-state reaction using TiO_2 anatase (Prolabo) as precursor, or by a sol−gel chemistry route in the case of TiP_2O_7, described in the appropriate sections of this paper. The morphology of the powders was controlled by scanning electron microscopy (FEG XL30), transmission electron microscopy (Philips CM12-100 kV), and BET[27] measurements.

Lattice parameters were determined first by full pattern matching of X-ray diffraction data. The crystal structures were determined from Rietveld refinement using the WinPLOTR/Fullprof suite,[28] from X-ray diffraction data recorded on a Bruker D5000 diffractometer ($CuK_{\alpha 1}$ radiation) and neutron diffraction data collected on the D20 line of ILL Grenoble, France. Table 1 summarizes the crystallographic parameters of the studied materials.

The compositions were tested as positive electrodes in Swagelok type cells assembled in an argon filled drybox. These homemade batteries were configured as Li metal/Whatman GF/D borosilicate glass fiber sheet saturated with a 1 M $LiPF_6$ in ethylene carbonate (EC)/dimethyl carbonate (DMC) (1:1 in weight) positive electrode cells. The composite positive electrodes were prepared by mixing the active material (AM) with 16.67 wt % of carbon Super P either in an agate mortar or in a ball-miller (SP, MMM Carbon, Belgium) to improve electronic contacts. Lithium insertion/extraction was monitored with a Mac-Pile automatic cycling/data recording system (Biologic SA, Claix, France) operating in galvanostatic intermittent titration technique (GITT) or potentiostatic intermittent titration technique (PITT) modes. A VMP device was also used for the signature curves recorded for $Li_xTiP_2O_7$ and $Li_{1+x}Ti_2(PO_4)_3$.

Electrochemically driven structural changes were followed by in situ X-ray diffraction for $Li_{1+x}TiPO_5$ ($0 \le x \le 0.8$), Li_xTiSO_5 ($0 \le x \le 0.8$), $Li_xTiP_2O_7$ ($0 \le x \le 1$), $Li_{1+x}Ti_2(PO_4)_3$ ($0 \le x \le 2$), and $Li_xNaTi_2(PO_4)_3$ ($0 \le x \le 1.8$). The cell used was that previously described elsewhere[29] with a plastic film of the positive electrode material deposited behind a beryllium window, which acted as the positive current collector. The preparation of the plastic films was done as previously reported for the plastic PLiON (Bellcore) technology[30] to which was added a preliminary ball-milling step of 30 min (SPEC ball-miller) to favor electrical contacts between the AM and carbon SP (83.3% of AM). The film contained 70 parts of the latter and 18 parts of dibutylphthalate (DBP) dispersed in 12 parts of (poly) vinylidene−hexafluoropropylene (PVdF−HFP) (Kynar FLEX, Elf Atochem NA). Once assembled, the cell was mounted on a Scintag diffractometer (Cu Kα radiation) operating in $\theta/2\theta$ Bragg−Brentano geometry or on a D8-Bruker diffractometer (CoK_α radiation, PSD counter) operating in θ/θ geometry. The cell was connected to a Mac-Pile system operating in GITT mode: 1 h of charge or discharge at C/10 regime interrupted by relaxing periods of 1−1.5 h during which the X-ray diffraction patterns were collected.

Chemical lithiations of TiP_2O_7, $LiTi_2(PO_4)_3$, and $NaTi_2(PO_4)_3$ were performed using a slight excess of *n*-BuLi (1.6 M) (reducing agent), previously diluted in a solution of hexanes. The reactions were maintained under constant stirring at ambient temperature in a flask kept in an argon filled glovebox for a period of 5−7 days, and washed several times with hexanes before drying under vacuum. Because of the moisture sensitivity of these lithiated phases, the XRD data were recorded using the same airtight cell as that used for the in situ studies. Chemical analysis performed at the Service Central d'Analyse du CNRS (Vernaison, France) concluded to formulas of $Li_{0.85}Ti_2P_2O_7$ and $Li_{3.00}Ti_2(PO_4)_3$ and $Li_{2.00}NaTi_2(PO_4)_3$.

3. Results and Discussion

3.1. Lithium Insertion into $TiSO_5$, $LiTiPO_5$, and Li_2TiSiO_5. Oxotitanium materials, expressed by the general formula Li_xTiXO_5 (X = S, P, and Si; $x = 0$, 1, and 2, respectively) were investigated. This family of compositions, with the same Ti/X ratio, was chosen to provide comparative data on how the Ti^{4+}/Ti^{3+} couple would be shifted by the inductive effect of S, P, and Si on the Ti−O bond.

(27) Brunauer, S.; Emmett, P. H.; Teller, E. *J. Am. Chem. Soc.* **1938**, *60*, 309.
(28) Roisnel, T.; Rodriguez-Carvajal, J. *WinPLOTR (June 2001)*, downloadable at: http://www-llb.cea.fr/fullweb/powder.htm.
(29) Patoux, S.; Masquelier, C. *Chem. Mater.* **2002**, *14* (5), 2334−2341..
(30) Tarascon, J.-M.; Gozdz, A. S.; Schmutz, C.; Warren, P. C. *Solid State Ionics*, **1996**, *86*, 49.

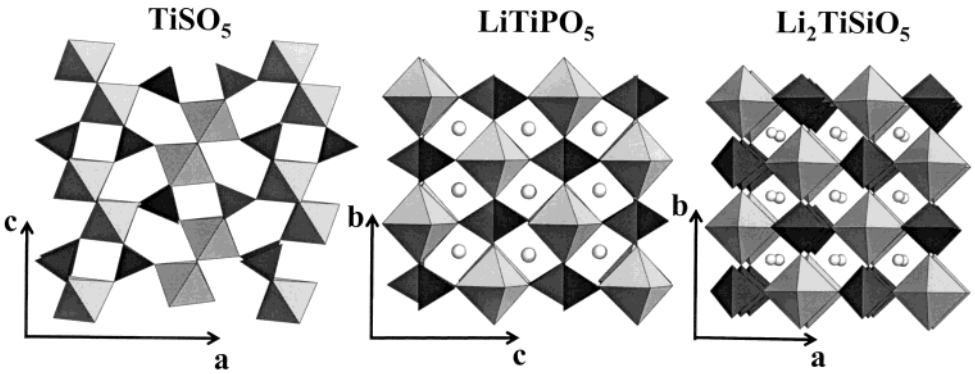

Figure 2. Views of the structures of Li_xTiXO_5 ($x = 0$, 1, 2 and X = S, P, Si, respectively) along the tunnels available for lithium ion diffusion. XO_4 tetrahedra in black. TiO_6 octahedra in gray.

$TiSO_5$ was prepared by dehydration at 673 K of commercial $TiSO_5 \cdot nH_2O$ (ALFA) with $n \approx 5.5$ as deduced from TGA. $TiSO_5$ can also be synthesized from titanium dioxide and sulfuric acid,[31] which, depending on the concentration, time, and temperature of reaction, leads to a highly hydrated $TiSO_5 \cdot nH_2O$ solid that dehydrates to $TiSO_5 \cdot H_2O$ and then to $TiSO_5$. $LiTiPO_5$ and Li_2TiSiO_5 were obtained at 1173 and 1373 K, respectively, from intimately mixed precursors LiH_2PO_4 (Aldrich, 99%), anatase TiO_2, $LiOH \cdot H_2O$ (Aldrich, min. 99%) − SiO_2 (PROLABO). Attempts to prepare compositions in the solid solution $Li_{1+x}TiP_{1-x}Si_xO_5$ failed. This may be due to the fact that $LiTiPO_5$ and Li_2TiSiO_5 do not crystallize in the same space group although their crystal structures are very closely related. The high temperature needed to proceed to the reaction of the SiO_2 precursor results in decomposing $LiTiPO_5$ into TiP_2O_7, $LiTi_2(PO_4)_3$, and other unknown compounds.

Figure 2 depicts the crystal structures of these 3 materials. The frameworks of Li_2TiSiO_5 and $LiTiPO_5$ are similar to those of α-VPO_5[32] and α-$NbPO_5$,[29] whereas $TiSO_5$ exhibits the bronzoid structure of β-$NbPO_5$.[33] The crystal structure of the dilithium titanosilicate Li_2TiSiO_5[34] consists of SiO_4 tetrahedra sharing all their corners with TiO_5 square pyramids, which can be viewed alternately as TiO_6 octahedra strongly distorted along the *c*-axis. The three-dimensional network may be described also as $TiSiO_5^{2-}$ layers separated by slabs of lithium perpendicular to the [001] direction. The lithium ions occupy all the octahedral cavities formed by two oxygen belonging to two SiO_4 tetrahedra and four oxygen belonging to two TiO_6 pseudo octahedra. $LiTiPO_5$[35] can be roughly considered as built from a similar arrangement of PO_4 tetrahedra and more regular TiO_6 octahedra running along the *a*-axis instead of the *c*-axis. The lithium content, twice less important than in the silicate phase, will have a strong impact on the electrochemical behavior during Li insertion. $TiSO_5$ (β-form) adopts the bronzoid form of β-$NbPO_5$,[29] which is described as the $m = 2$ member of the "monophosphate tungsten bronze with pentagonal tunnels" family of general formula $A_x(NbO_3)_{2m}(PO_2)_4$ (where A represents an alkaline ion, *m* is an integer, and *x* is charge compensating). The structure of β-$TiSO_5$ adopts an ReO_3-type arrangement made up by chains of TiO_6 octahedra separated by slabs of SO_4 tetrahedra delimiting pentagonal tunnels where the double strings of TiO_6 octahedra parallel to the *b*-axis are isolated, and linked to others only by tetrahedra.

Whereas a standard electrode preparation was sufficient for a satisfactory electrochemical cycling of the oxides described in section 3a, the fabrication of optimized Li_xTiXO_5/carbon SP electrodes required a ball-milling process to ensure good electronic contact.[15] The active material (AM) and carbon SP were mixed in the ratio 200 mg/40 mg (16.67% of carbon) for 30 min in a SPEX ball-miller that produces energetic shocks between particles and a stainless ball of ∼4 g inside a 40-mL container. The general features of the electrochemical insertion of lithium into the three materials are summarized in the GITT data of Figure 3.

Li_2TiSiO_5 does not insert more than 0.15 lithium ion per structural formula, even under the most gentle cycling conditions, down to 1 V vs Li^+/Li (Figure 3a). In Li_2TiSiO_5, all the tunnels along the chains of TiO_6 octahedra are already filled with lithium, contrary to $LiTiPO_5$, which in turn reversibly inserts more than 0.6 lithium at 1.50V vs Li^+/Li (Figure 3b). For $Li_{1+x}TiPO_5$, the overvoltage between the reduction (Red1) and the oxidation (Ox1) peaks is small under slow cycling rate with intermittent relax. Note though that only 0.5 Li ion could be inserted galvanostatically down to 1 V under a C/20 regime without relax period. Insertion in $LiTiPO_5$ is therefore kinetically limited by the difficulty in reaching the "lithium-stuffed" composition Li_2TiPO_5. The reaction is mostly reversible, as shown by the comparison between the areas of the Red1 and Ox1 peaks and the similar operating voltage on reduction and oxidation. Note that the operating equilibrium voltage (1.50 V) is not higher than that for the simple oxides. In situ XRD showed no displacement of the diffraction peaks of the pristine $LiTiPO_5$, which progressively vanished on discharge. The XRD pattern of the second growing phase is poorly defined, its main features being three broad diffraction peaks at $d = 3.315$ Å (most intense), $d = 3.015$ Å, and $d = 2.370$ Å. After $x \sim 0.6$ lithium inserted, very strong kinetic limitations witnessed by the important polarization of the cell prevent the total reduction of $LiTiPO_5$ into Li_2TiPO_5.

(31) Ahmed, M. A. K.; Fjellvag, H.; Kjekshus, A. *Acta Chem. Scand.* **1996**, *50*, 275−283.
(32) Gaubicher, J. Ph.D. Thesis. Université de Paris VI, 1998
(33) Gatehouse, B. M.; Platts, S. N.; Williams, T. B. *Acta Crystallogr.* **1993**, *49*, 428−435.
(34) Ziadi, A.; Thiele, G.; Elouadi, B. *J. Solid State Chem.* **1994**, *109*, 112−115.
(35) Robertson, A.; Fletcher, J. G.; Skakle, J. M. S.; West, A. R. *J. Solid State Chem.* **1994**, *109*, 53−59.

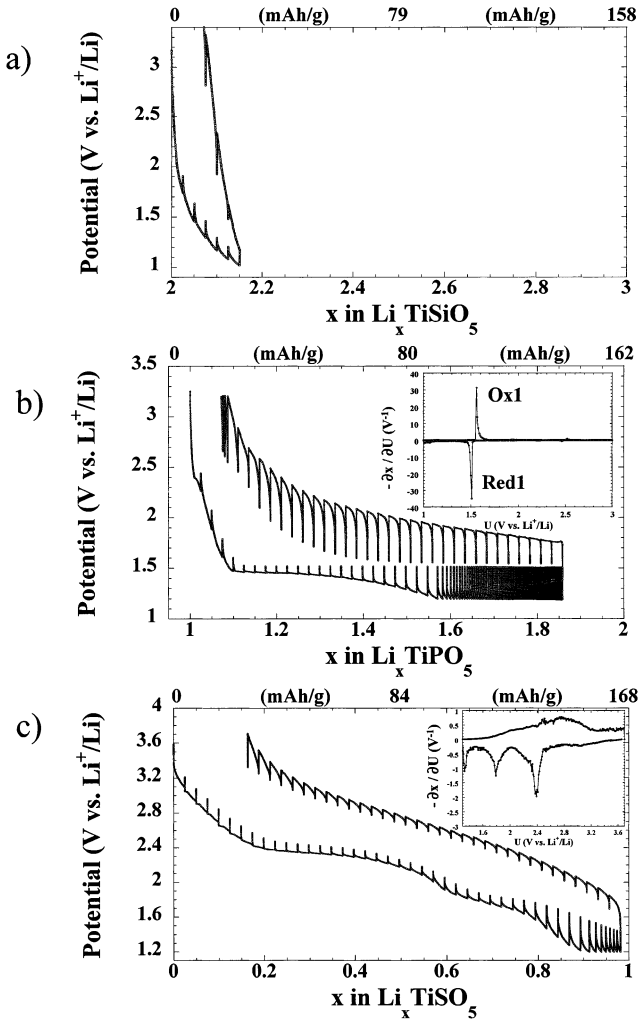

Figure 3. Potential−composition curves vs Li^+/Li of (a) Li_2TiSiO_5, (b) $LiTiPO_5$, and (c) $TiSO_5$, performed in a galvanostatic intermittent mode: regime of C/20 for 30 min and relax periods of 30 min. The insets display the incremental capacity voltammograms.

These limitations and the small operating voltage of the cell diminish the interest of such material as an electrode in Li batteries.

The GITT data of lithium insertion into the third member of the $TiXO_5$ series we investigated, namely $TiSO_5$, are presented in Figure 3c. Although this compound adopts a crystal structure slightly different from those of Li_2TiSiO_5 and $LiTiPO_5$ it is not too surprising to observe that the operating voltage of the Li_xTiSO_5/Li cell is significantly higher than for $Li_{1+x}TiPO_5$. This is once again a clear signature of the inductive effect in polyanionic structures, stronger when generated by SO_4^{2-} groups than when generated by PO_4^{3-} groups. As for $Li_xFe_2(XO_4)_3$ and Li_xVXO_5 compositions, the sulfate groups weaken considerably the covalency of the M−O bonds and thus increase the value of the $M^{n+}/M^{(n-1)+}$ redox couple vs Li^+/Li. This is easily monitored experimentally for isotypic structures, but more difficult to address when different crystal structures have to be compared. As mentioned by Gaubicher,[32] the overall inductive effect is weaker in MXO_5–type structures (M connected to 4 XO_4 groups) than in NASICON ones (M connected to 6 XO_4 groups). For this reason, as will be demontrated later, the operating voltage of Ti^{4+}/Ti^{3+} vs Li is not higher in $TiSO_5$ than in TiP_2O_7 or $LiTi_2(PO_4)_3$. When the cell is assembled, the value of the open circuit voltage of the system Li/Li_xTiSO_5 lies at about 3.5−3.7 V vs Li^+/Li for $x = 0 + \delta$. The potential decreases continuously first for $0 \le x \le 0.2$ prior to two-phase-like domain for $0.2 \le x \le 0.5$ at 2.5 V vs Li^+/Li. For $x \ge 0.5$, one observes a sharper decrease in the cell potential down to ∼1 V, where almost 1 lithium has been inserted in $LiTiSO_5$. On first charge up to 3.7 V, the voltage variation with x lithium extracted is much smoother, which could suggest that part of the redox processes encountered on first discharge is not reversible.

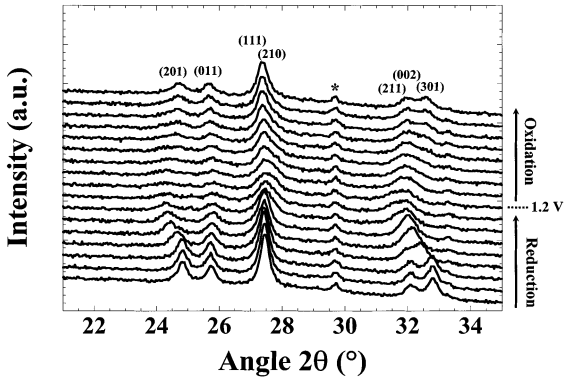

Figure 4. Evolution of the in situ X-ray diffraction patterns of an electrode of $TiSO_5$ during the insertion/extraction of lithium, under a GITT mode in the 3.4−1.2 V range vs Li^+/Li. Acquisition time of 1.25 h in the 20.00−44.00 2θ (°) angular range from a CoK_α radiation on a D8-Bruker diffractometer, equipped with a PSD counter. The asterisk indicates a diffraction peak coming from the hardware.

To check this point, an in situ X-ray diffraction experiment was carried out (Figure 4). The XRD patterns, collected at x increments of 0.1 in Li_xTiSO_5, correspond to the reversible insertion/extraction of 0.8 lithium ion down to 1.2 V vs Li^+/Li. Strong shifts of the (201) and (301) peak positions were observed, as well as a broadening of all the diffraction peaks during the first discharge (reduction). Figure 5 retraces the evolution of the cell parameters and volume during this process. From $x = 0$ to $x = 0.2$, no change was detectable, which suggests that, as we observed in several iron phosphates,[36] Li is first inserted within an amorphous matrix generated by the positive electrode ball-milling. Then, from $x = 0.2$ to $x = 0.4$, the sudden peak shift corresponds to a strong stretching of the **a** parameter (+2.1%), which could have been at first sight the signature of a two-phase region. Careful refinements showed though that the XRD patterns are much better fitted in a single phase model all along the $0.2 \le x \le 0.8$ domain. Globally, **a** and **c** increase, whereas **b** decreases, resulting in a global volume expansion of +2.6% from $x = 0.2$ to $x = 0.8$. This anisotropy in lattice parameters variation may be understood by the structural features of $TiSO_5$ (Figure 2). Reduction of Ti^{4+} into Ti^{3+} generates weaker electrostatic repulsions along [010], hence smaller **b** lattice parameter, which is the direction along which distorted TiO_6 octahedra share corners to generate infinite buckled ribbons. The global

(36) Wurm, C.; Morcrette, M.; Dupont, L.; Rousse, G.; Masquelier, C. *Chem Mater.* **2002**, *14* (6), 2701−2710.

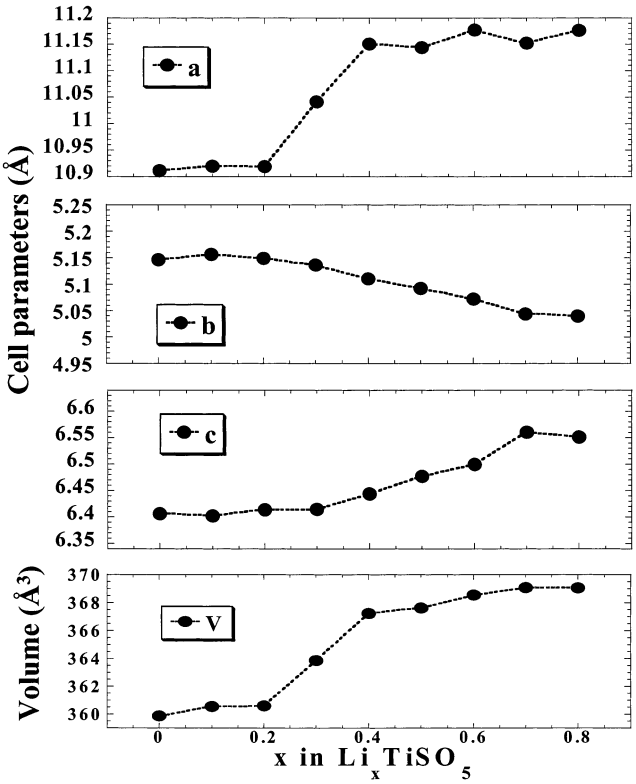

Figure 5. Refined cell dimensions of Li_xTiSO_5 ($0 < x < 0.8$) plotted against lithium content, using the full pattern matching (Le Bail) method from the in situ XRD patterns of Figure 4.

volume expansion on reduction of Ti^{4+} to Ti^{3+} is thus ensured by the stretching of the cell in the [100] and [001] directions.

The system Li/Li_xTiSO_5 is reversible on subsequent oxidation, as the XRD pattern of the pristine phase is mostly recovered after a full cycle, although the global intensity is slightly reduced. Under these in situ cycling conditions, we did not observe the large irreversibility (~0.2 lithium) that resulted from a discharge down to 1 V vs Li^+/Li. At low voltage, electrode degradation presumably results from departure of sulfate groups within the electrolyte. At this point, although the inductive effect of the SO_4 groups is beneficial to higher operating voltages compared to phosphates and oxides, it also induces weaker Ti−O bonds and thus weakens the structural stability of the electrode over cycling. As will be mentioned later (section 4. Discussion), better capacity retention was obtained when adjusting the operating voltage window between 3.7 and 1.3 V vs Li^+/Li. Corresponding galvanostatic voltage−composition curves, with several cutoff limits are presented in Figure 6. Interestingly, the internal impedance of the Li/Li_xTiSO_5 system decreases during cycling, which accounts for the good capacity retention from the second cycle to further cycles when the lower cutoff voltage is maintained above 1.2−1.3V vs Li^+/Li.

3.2 Lithium Insertion into TiP_2O_7. Pure TiP_2O_7 powders were prepared by two chemical routes. Classical solid state reaction consisted of mixing intimately TiO_2 and $NH_4H_2PO_4$ that were then progressively heated to 1273 K with intermittent grinding sequences. By this method, heterodispersed particles (~2 μm diameter for the smaller ones) were agglomerated. An

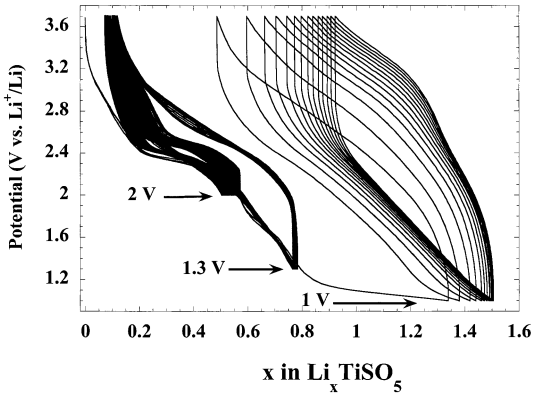

Figure 6. Cycling behavior of $TiSO_5$, under galvanostatic modes at current densities equivalent to a C/10 regime, for different discharge cutoff voltages and for the same upper cutoff voltage of 3.7 V vs Li^+/Li.

alternative route used a solution of Ti^{IV} isopropoxide (Aldrich, 97%) slowly added to an aqueous solution of diluted H_3PO_4 (Aldrich, 98%, stored at 269 K) to form a gel-like substance. The water and other alcoholic solvating species were evaporated overnight at 363 K before being heated at 1123 K for 1 day. This resulted in homogeneous and "individual" particles of smaller grain size (0.2−0.3 μm).

The crystal structure of TiP_2O_7 was recently determined[41] using XRD and NMR techniques, which demonstrated a structural disorder in a cubic $3 \times 3 \times 3$ superstructure by analogy to the other members of the $M^{4+}P_2O_7$ family (M = Si, Sn, Pb, Zr, etc.). Our refinement of the structure led to the same result. By using a unit cell parameter one-third smaller ($a = 7.877$ Å rather than 23.632 Å) numerous peaks were left unindexed. The structure is composed of diphosphate groups linked to TiO_6 octahedra in an NaCl-type arrangement which induces the well-known negative thermal expansion properties of these diphosphate materials.[37]

As seen by the GITT plot of Figure 7a, one lithium may be inserted into TiP_2O_7 down to 2.2 V vs Li^+/Li, corresponding to the reduction of Ti^{4+} to Ti^{3+}, with an irreversibility of ~10% on first charge. Two distinct redox processes, appearing as a sharp peak at 2.63 V in the derivative curve (inset of Figure 7a) and as a smoother one at 2.57 V, are clearly distinguished on both reduction and oxidation. In a first approach, the plateau at 2.63 V ($x = 0-0.5$) would correspond to a two-phase reaction between TiP_2O_7 (labeled A) and $Li_xTiP_2O_7$ ($x \sim 0.5$, labeled B), whereas the second process at 2.57 V is more complex, which probably includes a second two-phase domain (B′ + C) surrounded by two short solid-solution regions of both extreme compositions (B to B′ and C to C′). This proposed mechanism is further supported by the potentiodynamic intermittent experiment (Figure 7b). The recognizable signature responses of the current between the compositions TiP_2O_7 and $Li_xTiP_2O_7$ ($x \sim 0.5$) and in the $0.65 < x <$

(37) Sanz, J.; Iglesias, J. E.; Soria, J.; Losilla, E. R.; Aranda, M. A. G.; Bruque, S. *Chem. Mater.* **1997**, *9*, 996−1003.
(38) Hagman, L. O.; Kierkegaard, P. *Acta Chem. Scand.* **1968**, *22*, 1822−1832.
(39) Wang, S.; Hwu, S.-J. *J. Solid State Chem.* **1991**, *90*, 377−381.
(40) Wang, S.; Hwu, S.-J. *Chem. Mater.* **1992**, *4*, 589−595.
(41) Abrahams, S. C.; Bernstein, J. L. *J. Chem. Phys.* **1966**, *45*, 2745.

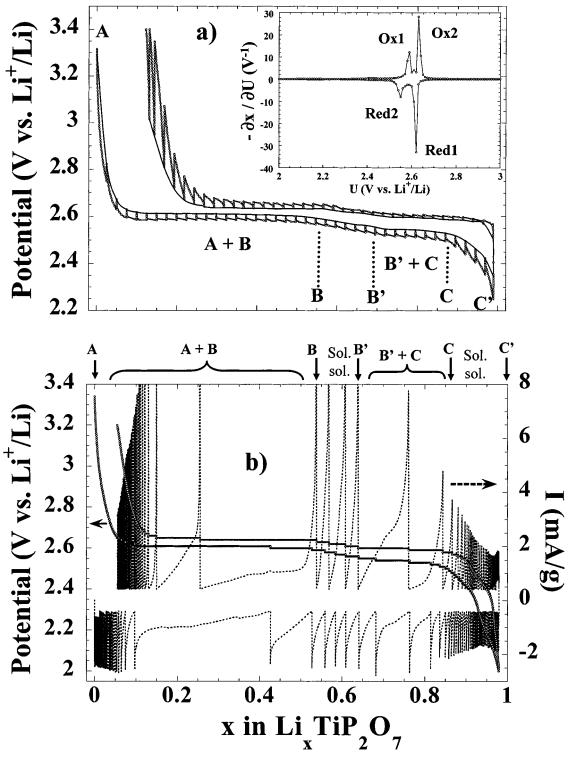

Figure 7. (a) Potential−composition curve of TiP_2O_7 performed in a galvanostatic intermittent mode at C/20 regime for 30 min and relax periods of 30 min in the 3.40−2.00 V range vs Li^+/Li. The inset plot draws the incremental capacity voltammogram. (b) Charge−discharge profile under a potentiodynamic intermittent titration mode (PITT) of the first cycle of TiP_2O_7 in the 3.40−2.00 V range vs Li^+/Li (I_{min} = 6.1 μA).

0.85 domain are characteristic of two-phase domains. Intermediate solid solution domains occur in the composition ranges $0.5 \leq x \leq 0.65$ and $x \geq 0.85$.

An in situ XRD experiment (Figure 8) was performed to confirm the presence of two-phase domains and solid solution regions, highlighting the existence of three distinct phases (A, B, and C) all along the reduction process. Within the "A−B" two-phase domain, the XRD peaks of TiP_2O_7 progressively vanish to the benefit of those of $Li_xTiP_2O_7$ ($x \sim 0.5$) at smaller 2θ angles, and we verified that the lattice constant **a** of both cubic TiP_2O_7 (a = 23.63(1) Å) and $Li_{0.5}TiP_2O_7$ (a = 23.79(1) Å) remains unchanged within this two-phase region. Then, the slight shifts of the diffraction peaks (deduced from the refinements) correspond to the "B−B′" solid solution $Li_xTiP_2O_7$ ($0.50 < x < 0.60-0.65$) with a = 23.79(1) Å to a = 23.84(1) Å. A second two-phase domain ("B−C") was then found for $\sim 0.6-0.65 < x < 0.85$, and, finally, a solid solution proceeded from $x \sim 0.85$ (a = 23.96(1) Å) to $x \sim 1$ (a = 23.98(1) Å). The formation of $Li_{0.955}TiP_2O_7$ at the end of discharge (a = 23.98(1) Å) corresponds to a global unit cell volume expansion of $\Delta V/V$ = + 4. 4% from the pristine material TiP_2O_7 (a = 23.63(1) Å).

We tried to prepare this new $LiTiP_2O_7$ composition by chemical reduction of TiP_2O_7 with *n*-BuLi, and, from chemical analysis, a solid of global composition $Li_{0.85}TiP_2O_7$ was obtained. A neutron diffraction pattern was collected at ILL at Grenoble (France) using an airtight cell made of vanadium to protect the material from air. Figure 9 retraces the full-pattern matching refinement of this pattern, which is compared to that of the pristine material. It shows that the lithiated phase we obtained was a mixture of B and C-type phases but we did not succeed in refining the atomic positions by the Rietveld method in these two separate phases. The average composition $Li_{0.85}TiP_2O_7$ found by chemical analysis corresponds to a mixture of 24% of $Li_xTiP_2O_7$ ($x \sim 0.50-0.65$) and 76% of $Li_xTiP_2O_7$ ($x \sim 0.85-1$). Note that the cell parameters are slightly different between the neutron data obtained on an intermediate lithiated phase and those found from the in situ experiment.

Moreover, the in situ data reveal the good reversibility of the system as the XRD pattern of the pristine material TiP_2O_7 is recovered at the end of the first oxidation. This is a common feature to many polyanionic framework structures built on phosphate groups that

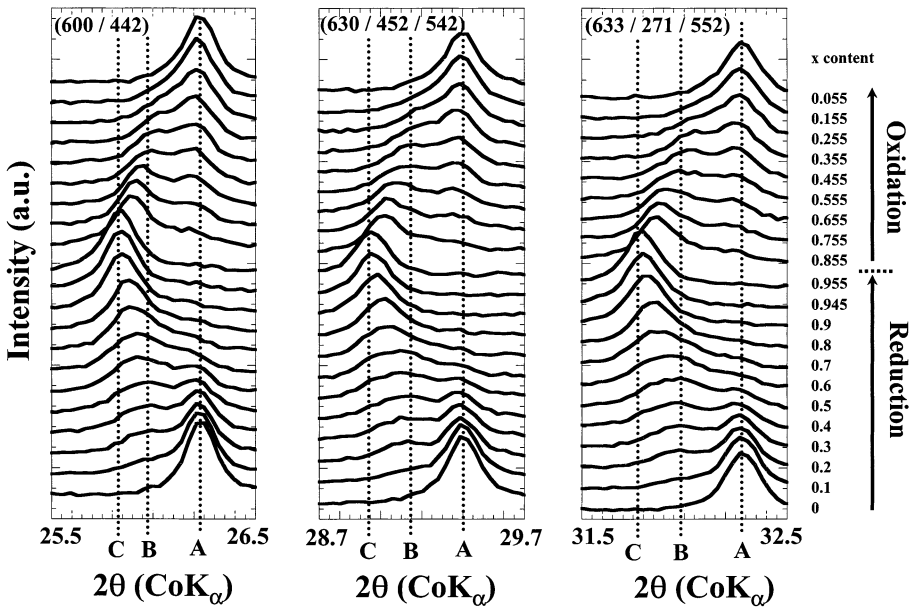

Figure 8. Selected regions of the X-ray diffraction patterns recorded in situ during the reduction/oxidation of an electrode of TiP_2O_7 between 3.40 and 2.00 V. Acquisition time of 1 h in the 18.00−40.00 2θ (°) range from a CoK_α radiation on a D8-Bruker diffractometer equipped with a PSD counter.

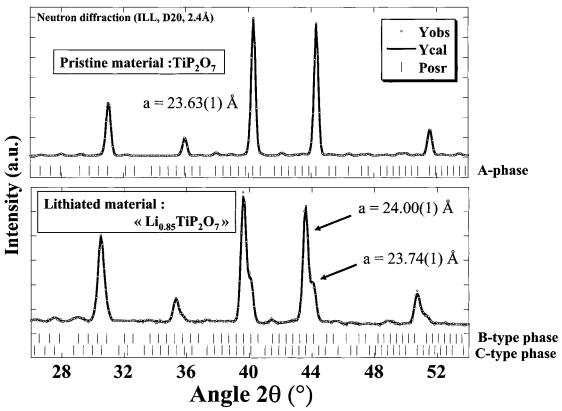

Figure 9. Neutron powder diffraction patterns of TiP_2O_7 and $Li_{0.85}TiP_2O_7$ performed at ILL at Grenoble on the high flux D20 beam with a 2.4 Å wavelength. The Rietveld method was used to refine the diffraction patterns.

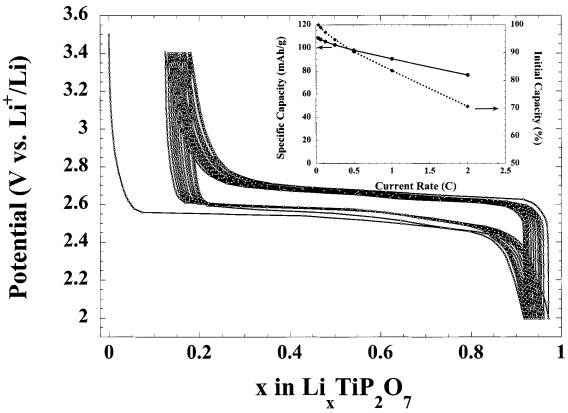

Figure 10. Charge−discharge profile under a galvanostatic mode at current density of C/10 (0.15 mAh) in the 3.40−2.00 V range vs Li^+/Li for TiP_2O_7. The rate capability curve of TiP_2O_7 is presented in the inset.

easily accommodate relatively large volume expansions/contractions over extensive electrochemical cycling. To account for this nice reversibility, electrochemical cycling was conducted in galvanostatic mode (C/10) between 3.4 and 2 V vs Li^+/Li (Figure 10). The reason for the irreversible capacity loss occurring on the first oxidation is not yet understood. The positive electrode material cycles then on ~0.8 lithium corresponding to a very stable capacity of 100 mAh/g of active material at an average potential of 2.6 V vs Li^+/Li. Note that the theoretical capacity of TiP_2O_7 is relatively small due to the weight penalty of the 2 diphosphate groups per titanium, whereas the response of TiP_2O_7 under various current rates, depicted through the signature plot of Figure 10 is reasonable for a polyanionic structure.

3.3 Lithium (or Sodium) Insertion into $ATi_2(PO_4)_3$ (A = Li, Na). The two NASICON compositions $NaTi_2(PO_4)_3$ and $LiTi_2(PO_4)_3$ were synthesized following a classical solid-state reaction. TiO_2, $NH_4H_2PO_4$, and NaH_2PO_4 (or LiH_2PO_4) precursors were mixed and heated to 573 K at a slow heating rate (0.5 K/min) to evaporate H_2O and NH_3, then to 873 K (24 h), and finally to 1273 K (48 h). Pure and well-crystallized white powders were obtained. Their X-ray diffraction patterns were fully indexed in the $R\bar{3}c$ space group with unit-cell parameters very close to those previously reported by Delmas.[10]

$LiTi_2(PO_4)_3$ and $NaTi_2(PO_4)_3$ are isostructural with $NaZr_2(PO_4)_3$[38] and adopt the well-known NASICON-type structure consisting of a three-dimensional network made up of tetrahedra sharing all their corners with octahedra and vice versa to form the so-called "lantern" units, all oriented in the same direction (along the **c**-axis) (Figure 11a). In the space group $R\bar{3}c$, the alkaline ions fully occupy the octahedral M1 site (6b), whose coordinates are (0; 0; 0) whereas Ti, P, O1, and O2 are in the Wyckoff positions (12c), (18e), (36f), and (36f), respectively. Note that the crystal structures of mixed-valence $Ti^{III/IV}$ phosphates $Li_{1+x}Ti_2(PO_4)_3$ single crystals prepared at high temperature were solved by Wang.[39,40] Such compositions do not adopt the NASICON structure (when $x > 0.3$) but the $Sc_2(WO_4)_3$-type structure[41] where the $[Ti_2(PO_4)_3]$ lanterns are oriented differently.

Fifteen years ago, Delmas[10,11] was the first to show the possible lithium or sodium insertion into $LiTi_2(PO_4)_3$ and $NaTi_2(PO_4)_3$, respectively, according to a two-phase mechanism between the pristine materials $ATi_2(PO_4)_3$ (A = Li or Na) and the end members $A_3Ti_2(PO_4)_3$ into which titanium is at the oxidation state +III. At this early stage of investigation, lithium was thought to occupy the M2 site of the NASICON structure in $Li_3Ti_2(PO_4)_3$, while the M1 site was empty. This accounted for the remarkable increase in the c/a ratio, when going from $LiTi_2(PO_4)_3$ to $Li_3Ti_2(PO_4)_3$, due to stronger electrostatic repulsions between $[Ti_2(PO_4)_3]$ lanterns along [001] when the M1 site, located halfway between two lanterns, is emptied. Recently, the determination of the crystal structure of the isostructural compound $Li_3Fe_2(PO_4)_3$,[42] obtained by ion exchange from the parent $Na_3Fe_2(PO_4)_3$, showed that the correct space group was R-3 rather than R-3c (presence of (101), (003), and (303) reflections), and that lithium was indeed located into a set of tetrahedral sites, labeled M3, shifted by ~0.8 Å along [001] from the M2 position. The possibility of lithium location into such a site had been previously mentioned by Boireau et al.[43] who determined the crystal structure of $Li_{3.5}Cu_{0.5}Ti_2(PO_4)_3$. Even more recently,[12] Delmas' group discovered, from a careful investigation coupling solid-state Li NMR and powder neutron diffraction, that the situation is even more complex. In $Li_3Ti_2(PO_4)_3$ lithium is distributed on two similar tetrahedral sites, M3′ and M3″, occupied in the ratio $^2/_3$ and $^1/_3$, respectively[12] (Figure 11b).

As previously reported by Delmas[10] and Aatiq,[12] $LiTi_2(PO_4)_3$ may reversibly insert two lithium ions, operating on the Ti^{4+}/Ti^{3+} at 2.48 V vs Li^+/Li, according to a two-phase mechanism between $LiTi_2(PO_4)_3$ and $Li_3Ti_2(PO_4)_3$. As shown in Figure 12a, and contrary to the electrochemical data of ref 12[12], our electrode preparation (ball-milling with carbon) allowed the almost complete reversible insertion of lithium with extremely small cell polarization for more than 80% of the insertion range, also expressed by the narrow potential gap between the Ox 1 and Red 1 peaks of the PITT derivative curve (inset of Figure 12a).

The two-phase mechanism is further exemplified by the bell-shape current response depicted in Figure 12b

(42) Masquelier, C.; Wurm, C.; Rodriguez-Carvajal, J.; Gaubicher, J.; Nazar, L. *Chem. Mater.* **2000**, *12*, 525−532.
(43) Boireau, A.; Soubeyroux, S. L.; Olazcuaga, R.; Delmas, C.; Le Flem, G. *Solid State Ionics* **1993**, *63−65*, 484−487.

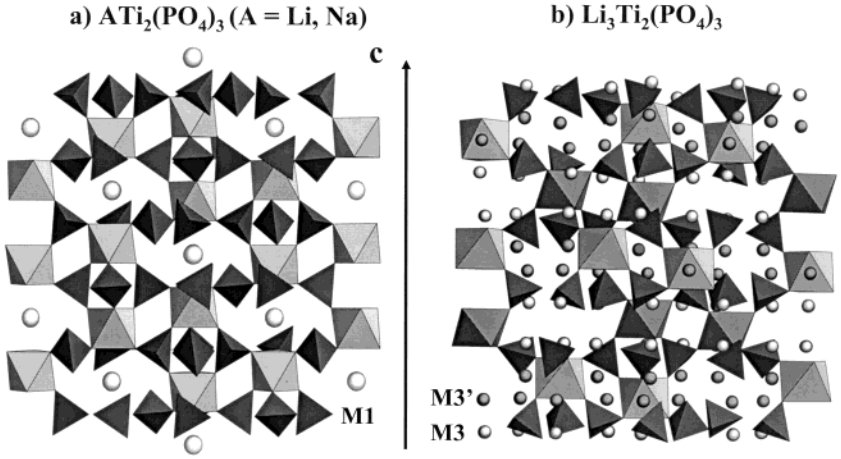

Figure 11. Structure of the NASICON materials $ATi_2(PO_4)_3$ (A = Li, Na) and $Li_3Ti_2(PO_4)_3$ viewed along [110]. The lithium positions in $Li_3Ti_2(PO_4)_3$ were communicated by ref 12[12].

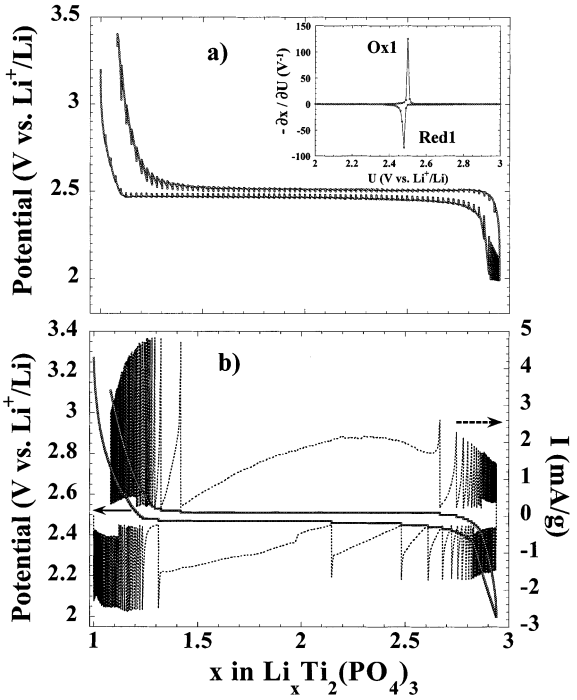

Figure 12. (a) Potential−composition curve of $LiTi_2(PO_4)_3$, performed in a galvanostatic intermittent mode at C/20 regime for 30 min and relax periods of 30 min in the 3.40−2.00 V range vs Li^+/Li. The inset plot draws the incremental capacity voltammogram. (b) Charge−discharge profile under a potentiodynamic intermittent titration technique (PITT) of the first cycle of $LiTi_2(PO_4)_3$ in the 3.40−2.00 V range vs Li^+/Li (I_{min} = 3.8 μA).

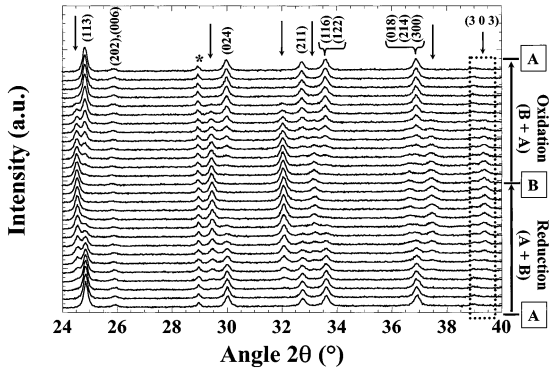

Figure 13. Evolution of the in situ X-ray diffraction patterns of an electrode of $LiTi_2(PO_4)_3$ during the first cycle under a GITT mode between 3.40 and 2.00 V vs Li^+/Li. Acquisition time of 1.5 h in the 20.00−42.00 2θ (°) window from a Cu Kα radiation on a Scintag diffractometer. The peak positions of the growing second phase are indicated by vertical arrows. The asterisk indicates a diffraction peak of the hardware.

and by the X-ray diffractograms of Figure 13 that were recorded in situ over a whole reduction/oxidation cycle. As shown for related compounds,[15] the single-phase insertion domain for $x < 0.15$ corresponds to lithium insertion into an $LiTi_2(PO_4)_3$ matrix that is mostly amorphous, and that was generated by the energetic ball-milling procedure necessary for the electrode preparation. Absolutely no change of lattice parameters of either $LiTi_2(PO_4)_3$ ($R\bar{3}c$, a = 8.508(1) Å, c = 20.833(6) Å) or $Li_3Ti_2(PO_4)_3$ (R3, a = 8.390(1) Å, c = 22.886(2) Å) was detected from refinements of the XRD patterns all along the insertion plateau. For $Li_3Ti_2(PO_4)_3$, the appearance of an XRD peak at around $2\theta \sim 39.0°$ (d = 2.30 Å, (303)) indicates that the space group $R\bar{3}c$ (into which $LiTi_2(PO_4)_3$ crystallizes) is no longer valid. A parallel can thus be made between $Li_3Ti_2(PO_4)_3$ and the NASICON form of $Li_3Fe_2(PO_4)_3$ (space group $R\bar{3}$, prepared by ion exchange from $Na_3Fe_2(PO_4)_3$). As already mentionned, one of us showed from neutron diffraction[42] that in NASICON $Li_3Fe_2(PO_4)_3$ lithium was located into a tetrahedral site, labeled M_3, displaced into the M_2 cavity of the NASICON framework by ∼0.8 Å along [001]. The very nice reversibility of this two-phase reaction is demonstrated by the XRD pattern recorded at the end of oxidation after a full cycle.

To confirm the possible isotypy between $Li_3Ti_2(PO_4)_3$ and $Li_3Fe_2(PO_4)_3$, we measured a neutron diffraction pattern (at ILL-Grenoble, D20 diffractometer, λ = 2.4 Å) of a large quantity of $Li_3Ti_2(PO_4)_3$ obtained through chemical lithiation with n-BuLi of $LiTi_2(PO_4)_3$. In the course of our study, we were informed by Ménétrier[12] that the location of lithium ions in $Li_3Ti_2(PO_4)_3$ is more complicated than originally thought and slightly different from that of $Li_3Fe_2(PO_4)_3$. From ^{7}Li NMR and powder neutron diffraction, Aatiq et al. showed indeed that lithium was not only located into the M_3 site of the $Li_3Fe_2(PO_4)_3$ structure but into two M_3 and M_3' sites with occupancy rates of $^2/_3$ and $^1/_3$, respectively. The Rietveld refinement of our neutron diffraction data showed no significant improvement in the reliability

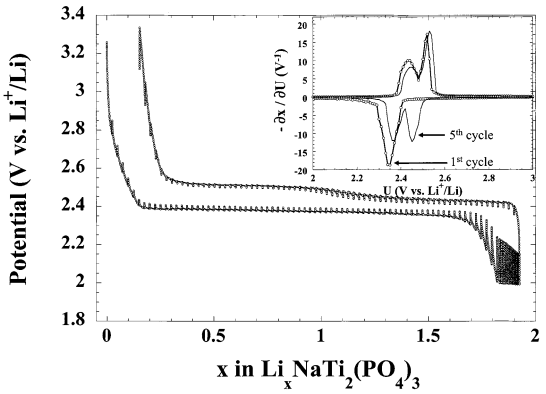

Figure 14. Potential−composition curve of $NaTi_2(PO_4)_3$, performed in a galvanostatic intermittent mode at C/20 regime for 30 min and relax periods of 30 min in the 3.40−2.00 V range vs Li^+/Li. The inset plot represents the incremental capacity voltammogram over the five first cycles, which resulted in an accelerated PITT measurement (I_{min} equivalent to a C/20 regime).

factors by using such a lithium distribution compared to the occupation of the M3 site only. Therefore, as demonstrated in ref 12, NMR was the key to detect such an original lithium distribution within the NASICON framework. In the $R\bar{3}$ space group description and by using the M_3 and M_3' sites for lithium location, the crystal structure (Figure 11b) features of $Li_3Ti_2(PO_4)_3$ are very similar to those described extensively for $Li_3Fe_2(PO_4)_3$[42]: (i) alternance of long and short Ti−Ti distances along [001], (ii) strong increase in the c/a ratio due to the absence of lithium into the M_1 site, (iii) LiO_4 tetrahedra connected via corners to form Li_6O_{18} rings, (iv) smaller distortions of TiO_6 octahedra, and(v) strong anisotropic displacement factors of lithium, with high mobility perpendicular to [001].

As shown in Figure 14, the isotypic composition $NaTi_2(PO_4)_3$ is also active toward the electrochemical insertion of lithium ions as 0.9 lithium per titanium could be inserted on first discharge through a two-phase insertion process, located this time at 2.40 V vs Li^+/Li. The two-phase mechanism is nicely demonstrated by the XRD patterns of Figure 15 recorded in situ at various stages of discharge and charge. As only 1.8 lithium could be inserted in the structure, small diffraction peaks of the starting compositions $NaTi_2(PO_4)_3$ are still observed at the end of discharge (cross markers). Interestingly, the intercalation voltage (2.4 V) is 0.1 V lower than that for the Li/ $LiTi_2(PO_4)_3$ cell, which may be a signature of thermodynamic limitations of lithium insertion into this Na-containing structure and/or Na^+-Li^+ repulsive interactions. Within the NASICON structure of the starting material $NaTi_2(PO_4)_3$, sodium is indeed located in the octahedrally coordinated M1 site, fully occupied, and Li insertion can proceed only through the partial filling of the M2/M3 sites. This requires displacement of both Li^+ and Na^+ along the M2-M1-M2 3-D diffusion pathways, which is unfavourable, as sodium shows a strong preference for the M1 site. The solid obtained at the end of discharge is a mixture of a few remaining unreacted $NaTi_2(PO_4)_3$ and a new phase $Li_2NaTi_2(PO_4)_3$, indexed in the space group R3 with lattice parameters a = 8.40(1) Å and c = 22.86(2) Å. Interestingly, one notes that the c/a ratio increases when going from $NaTi_2(PO_4)_3$ to $Li_2NaTi_2(PO_4)_3$, which suggests that part of the

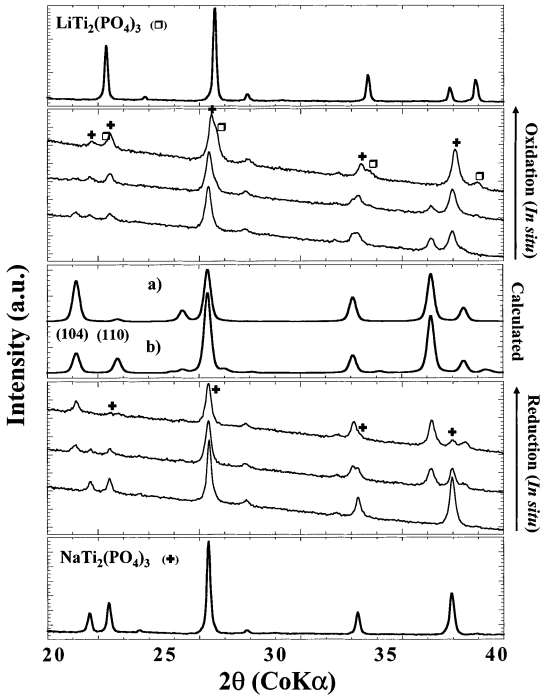

Figure 15. Experimental and calculated XRD patterns (CoK_α radiation) of $A_xTi_2(PO_4)_3$ compositions. Those of $NaTi_2(PO_4)_3$ (bottom) and $LiTi_2(PO_4)_3$ (top) are experimental patterns obtained from pristine powders, recorded overnight. In the middle are plotted calculated patterns of $Li_2NaTi_2(PO_4)_3$ with different Na^+ distributions: (a) Na^+ on M2 site and (b) Na^+ on M1 site. Below and above the calculated patterns are plotted selected experimental in situ XRD patterns recorded during reduction and oxidation in the Li/$NaTi_2(PO_4)_3$ system.

sodium ions have migrated from the M1 to the M2 sites of the NASICON structure. To verify this, we plotted on Figure 15 the calculated XRD patterns of two hypothetical $Li_2NaTi_2(PO_4)_3$ structures with sodium distributions of (a) Na^+ on M2 site or (b) Na^+ on M1 site. These two distributions significantly alter the intensity ratio between the (104) and (110) diffraction peaks, for instance, and our experimental in situ XRD pattern of $Li_2NaTi_2(PO_4)_3$ suggests that sodium is mostly located on the M2 site ((a) model). These results are only qualitative as we could not perform satisfactory Rietveld refinement of the structure: the beryllium window of the cell significantly diminishes the observed intensities at low 2θ values. However, they are further supported by a complementary experiment that we conducted on sodium insertion into $NaTi_2(PO_4)_3$.[44]

Having reached, on first discharge, the composition $\sim Li_2NaTi_2(PO_4)_3$ through an apparent single-phase process at 2.40 V vs Li^+/Li, the first oxidation proceeds through two distinct plateaus (Figure 14). One legitimate question was which (of Li^+ or Na^+) would be extracted first from the structure on oxidation? The first oxidation process (Ox1) is located at 2.40 V vs Li^+/Li, and is the reversible signature of the plateau (Red1) observed during the first reduction $NaTi_2(PO_4)_3 \leftrightarrow Li_2NaTi_2(PO_4)_3$. The second oxidation plateau (Ox2) is located at 2.48 V vs Li^+/Li, which corresponds to the operating voltage for the two-phase reaction $LiTi_2(PO_4)_3 \leftrightarrow Li_3Ti_2(PO_4)_3$. At this point, from the values of the

(44) Huang, S. Y.; Kavan, L.; Exnar, I.; Grätzel, M. *J. Electrochem. Soc.* **1995**, *142*, 142−144.

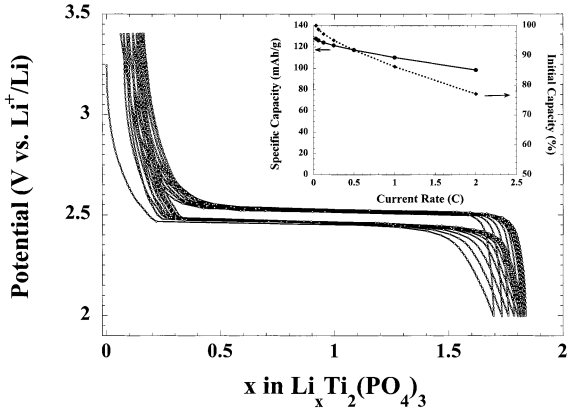

Figure 16. Charge−discharge profile under galvanostatic mode at current density of C/10 (0.15 mAh) in the 3.40−2.00 V range vs Li^+/Li for $LiTi_2(PO_4)_3$. The rate capability curve of $LiTi_2(PO_4)_3$ is presented in the inset.

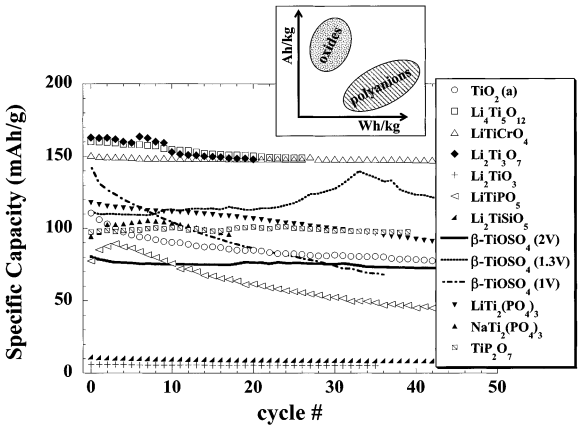

Figure 17. Specific capacity plots corresponding to all the materials discussed in the present paper with their potential range. For all the tests, the cycling rate used is C/10.

redox potentials measured on oxidation, our interpretation is that the two above reactions occur in sequence in the electrode, thus forming at the end of charge a mixture of y $LiTi_2(PO_4)_3$ and (1-y) $NaTi_2(PO_4)_3$. This is indeed what we observe from the XRD pattern of the end product after a full cycle, where diffraction peaks of both $LiTi_2(PO_4)_3$ and $NaTi_2(PO_4)_3$ are indexed (Figure 15) (cross and full-circle markers). If this proposed mechanism is correct, sodium has to be electrochemically extracted out of $Li_2NaTi_2(PO_4)_3$ or, more probably, partly substituted by lithium coming from the electrolyte through ion exchange reaction. We did verify (quantitatively), from energy dispersion spectroscopy analysis on electrodes at various stages of charge and after a series of cycles, that the electrode contained less and less sodium over cycling.

The observation of two distinct redox steps on discharge #2 supports this mechanism. The mixture y $LiTi_2(PO_4)_3 + (1 - y)\ NaTi_2(PO_4)_3$, which was reached after the first oxidation, inserts lithium at two redox potentials of 2.38 and 2.47 V vs Li^+/Li, i.e., to reach a final composition at the end of discharge #2 of ∼y $Li_3Ti_2(PO_4)_3 + (1 - y)\ Li_2NaTi_2(PO_4)_3$. As ion exchange $Na^+ \leftrightarrow Li^+$ continues to proceed, the global composition of the electrode tends to lower contents of sodium, which is witnessed by the incremental capacity plots in the inset of Figure 14: the areas of the reduction and oxidation peaks at 2.40 V ($NaTi_2(PO_4)_3 - Li_2NaTi_2(PO_4)_3$) decrease for the benefit of those at 2.50 V ($Li_3Ti_2(PO_4)_3 - LiTi_2(PO_4)_3$). Note that we verified that significant ion exchange between Li^+ from the electrolyte and Na^+ from $NaTi_2(PO_4)_3$ occurred by immersing the solid for several days in a large volume of $LiPF_6$ in EC/DMC.

Finally, Figure 16 reports the cycling curve of the $LiTi_2(PO_4)_3$ electrode, with the signature curve in the inset, similarly to what was obtained for TiP_2O_7 (Figure 10). This demonstrates once again the very nice stability of the NASICON framework toward reversible lithium insertion. Despite a lower voltage, $LiTi_2(PO_4)_3$ presents slightly higher specific capacity and capacity retention upon increasing cycling rate than TiP_2O_7. For instance, at a regime of 2C, about 77% of the initial capacity was delivered, which is almost 100 mAh/g.

4. Discussion and Conclusion

Several workers, as Padhi et al., showed that the potential of the redox couples of the transition metal elements (i.e., Ti^{4+}/Ti^{3+}) in polyanionic structures are affected by both the nature and the amount of the surrounding polyanionic groups. In the present case, XO_4 groups generate higher ionicity in Ti−O bonds due to the relocation of the electrons from the antibonding level of the 3d-element to the acceptor levels of the polyanion. Thus, potential difference between the Fermi level of lithium and the empty antibonding levels of titanium increases compared to that of simple oxides, which results in a higher operating voltage of the electrochemical cell.

From this study we can provide a wide comparison of average voltages vs Li^+/Li for the Ti^{4+}/Ti^{3+} redox couple in titanium oxides, phosphates, silicates, and sulfates. Within the phosphate compositions, the potential raises from 1.5 to 2.6 V vs Li^+/Li from $LiTiPO_5$ (Ti/P = 1) to TiP_2O_7 (Ti/P = 0.5), respectively. The average potential of the NASICON materials ($LiTi_2(PO_4)_3$ and $NaTi_2(PO_4)_3$, i.e., Ti/P = $^2/_3$), is located around 2.4−2.5 V vs Li^+/Li. $LiTiPO_5$ shows a much smaller insertion voltage than the other phosphates. This may be explained by the polyhedral environment of the TiO_6 octahedra. In $LiTiPO_5$, each TiO_6 octahedron is surrounded by 4 PO_4 tetrahedra only and 2 TiO_6 octahedra, whereas 6 PO_4 tetrahedra surround one TiO_6 octahedron in TiP_2O_7 and $ATi_2(PO_4)_3$ (A = Li, Na). Structural limitations due to the limited interstitial space left available in $LiTiPO_5$ are also at the origin of the difficulty in inserting more lithium. Li_xTiSO_5 showed an operating voltage vs Li^+/Li significantly bigger than for $Li_{1+x}TiPO_5$ due to the stronger inductive effect of SO_4 groups compared to that of PO_4 groups.

To conclude, we plotted in Figure 17 the capacity retention over 40 cycles of all the Ti-containing materials evaluated in this study. Despite the fact that most of the oxides provide a higher specific capacity (Ah/kg), the polyanionic materials possess a higher energy density (Wh/kg) (inset of Figure 17). Such study may be useful for offering a large range of material from which to choose, depending on the application envisaged. For example, Huang et al.[44] proposed the use of

anatase TiO_2 as a negative electrode for $LiCoO_2/TiO_2$ batteries. Similarly, the $LiFePO_4/Li_4Ti_5O_{12}$ system could be considered for providing a 2V Li-ion battery. TiP_2O_7 or $LiTi_2(PO_4)_3$ are interesting positive electrode materials for 2.5−2.6 V polymer lithium batteries containing Li at the negative electrode.

Acknowledgment. We thank Dr. G. Rousse for collecting the neutron diffraction data and for fruitful discussions. We also thank M. Ménétrier and C. Delmas for sharing their results on $LiTi_2(PO_4)_3$ and J. B. Leriche for designing a new in situ XRD cell.
CM0201798